


TOOLBOX

Single organelle dynamics linked to 3D structure by correlative live-cell imaging and 3D electron microscopy

Job Fermie^{1,2}  | Nalan Liv¹ | Corlinda ten Brink¹ | Elly G. van Donselaar¹ |
Wally H. Müller³ | Nicole L. Schieber⁴ | Yannick Schwab⁴ | Hans C. Gerritsen² |
Judith Klumperman¹

¹Section Cell Biology, Center for Molecular Medicine, University Medical Center Utrecht, Utrecht University, Utrecht, The Netherlands

²Section Molecular Biophysics, Debye Institute for Nanomaterials Science, Utrecht University, Utrecht, The Netherlands

³Section Cryo-EM, Department of Chemistry, Utrecht University, Utrecht, The Netherlands

⁴Electron Microscopy Core Facility, EMBL Heidelberg, Heidelberg, Germany

Correspondence

Judith Klumperman, Section Cell Biology, Center for Molecular Medicine, University Medical Center Utrecht, Utrecht University, Heidelberglaan 100, 3584CX Utrecht, The Netherlands.

Email: j.klumperman@umcutrecht.nl

Funding information

Stichting voor de Technische Wetenschappen, Grant/Award number: 12715

Live-cell correlative light-electron microscopy (live-cell-CLEM) integrates live movies with the corresponding electron microscopy (EM) image, but a major challenge is to relate the dynamic characteristics of single organelles to their 3-dimensional (3D) ultrastructure. Here, we introduce focused ion beam scanning electron microscopy (FIB-SEM) in a modular live-cell-CLEM pipeline for a single organelle CLEM. We transfected cells with lysosomal-associated membrane protein 1-green fluorescent protein (LAMP-1-GFP), analyzed the dynamics of individual GFP-positive spots, and correlated these to their corresponding fine-architecture and immediate cellular environment. By FIB-SEM we quantitatively assessed morphological characteristics, like number of intraluminal vesicles and contact sites with endoplasmic reticulum and mitochondria. Hence, we present a novel way to integrate multiple parameters of subcellular dynamics and architecture onto a single organelle, which is relevant to address biological questions related to membrane trafficking, organelle biogenesis and positioning. Furthermore, by using CLEM to select regions of interest, our method allows for targeted FIB-SEM, which significantly reduces time required for image acquisition and data processing.

KEYWORDS

correlative light-electron microscopy, endolysosomal system, focused ion beam scanning electron microscopy, organelle dynamics, time-lapse microscopy, volume electron microscopy

1 | INTRODUCTION

Correlative light-electron microscopy (CLEM) comprises a collection of techniques that integrate light and electron microscopic data from a single sample, thereby combining the strengths of the two techniques. CLEM uses the large field of view of the light microscope (LM) to search for regions of interest (ROI), that is, rare or transient phenotypes or specific subpopulations of cells within a complex tissue, and combines this with electron microscopy (EM) for subsequent ultrastructural context investigation. Using fluorescence microscopy (FM) as LM approach, CLEM can in addition be used to infer molecular information to EM images. EM on the other hand is the only method to directly visualize membranes at high resolution, allowing the visualization of the compartment of interest as well as its

ultrastructural context. A powerful but also highly challenging CLEM approach is the combined use of live-cell FM and EM. Live-cell CLEM links subcellular dynamics to ultrastructural information, two parameters that are conventionally studied in separate samples. Consequently, our understanding of organelles is based on an average of dynamic data and an average of ultrastructural data. The live-cell CLEM method presented here has the potential to unequivocally resolve transient interactions between molecularly identified organelles, by combining dynamic recordings of subcellular compartments with ultrastructural snapshots of the exact same compartments.

For live-cell CLEM, live-cell data can be obtained using various FM techniques such as widefield, confocal or super-resolution, depending on the research question and kinetics and size of objects of interest. After imaging, the material is generally chemically fixed, and embedded

in resin or prepared for cryosectioning.^{1–4} Alternatively, samples are cryo-immobilized by either plunge freezing or high-pressure freezing. Samples can then be observed by cryo-FM and cryo-electron tomography (cryo-ET),⁵ or freeze substituted and resin embedded, after which the samples are observed at room temperature.^{6–8} Most strategies then rely on serial sectioning combined with transmission electron microscopy (TEM) to find back the ROI in EM.^{3,4,9–11} Despite its frequent use, serial sectioning is labor intensive, and suffers from several problems, including material loss, deformation of sections and difficulty with registration of consecutive sections.

Recently, scanning EM (SEM)-based approaches have emerged as alternative tools to serial sectioning and TEM.¹² By improvements in resolution and detector sensitivity, state of the art SEM systems can be used to study intracellular structures, at a slightly lower resolution than TEM. This has led to rapid developments in array tomography (AT),¹³ serial block face SEM (SBF-SEM)¹⁴ and focused ion beam SEM (FIB-SEM),^{15,16} techniques that are often referred to as volume EM since they yield information in 3D. In AT manually or automatically cut serial sections are collected on conductive supports, and automatically imaged in a SEM to reconstruct 3D structures. In SBF-SEM sectioning occurs in the SEM vacuum chamber, by use of a miniaturized ultramicrotome and diamond knife. In FIB-SEM, a highly focused gallium ion beam ablates a thin layer of the sample after which the newly exposed surface is imaged with the scanning electron beam. The system repeats this cycle for hundreds or thousands of slices until the volume of interest is imaged, generating imaged volumes that can reach upwards of $10^6 \mu\text{m}^3$ in state of the art systems.^{17,18} Of these volume EM techniques FIB-SEM provides the highest resolution in Z (4 nm), making it the technique of choice for imaging subcellular structures where visualization of morphological details is essential to establish their identity.^{18,19} Moreover, since the gallium ion beam is precisely controlled, it can be used to target specific ROIs for imaging, which reduces the time for imaging and data processing. This is important since FIB-SEM imaging is time consuming (on average 2–5 days of image acquisition per cell) and destructive (individual slices are destroyed during imaging). It is therefore highly advantageous to precisely select the ROI before starting image acquisition. This can be achieved through CLEM.

In previous studies demonstrating the ability to combine live-cell FM with either FIB-SEM or SBF-SEM,^{2,20,21} live-cell FM was primarily used as a method to identify a sporadic event within a prolonged time period. Here, we present a correlative live-cell FM to volume EM approach that for the first time links characteristic dynamic behavior of a single organelle to a complete analysis of its ultrastructural characteristics and does so in the context of its cellular surroundings. To reach this goal, we integrated known protocols for live-cell imaging, CLEM and FIB-SEM in such a way that we obtained an optimal pipeline for viewing single organelles from live FM to 3D FIB-SEM. We apply our method to the endolysosomal system, a complex and dynamic system of interacting membranes. By real time tracking of single endolysosomal compartments over several minutes and retracing these same compartments in EM, we show that live-cell imaging combined with FIB-SEM provides a powerful way to integrate dynamic, structural and morphological parameters into one single organelle. Moreover, the use of CLEM enables the selection of

small, well-defined ROIs for examination by FIB-SEM, thereby greatly reducing imaging time and volume of an ROI (from 2–5 days per cell to 24–36 hours per ROI).

2 | RESULTS

2.1 | Optimized correlation of live-cell fluorescence and FIB-SEM of single organelles

The endolysosomal system coordinates multiple processes in the cell: degradation of biomaterials obtained by endocytosis or autophagy, nutrient sensing, signaling and exocytosis.²² Endocytosed cargo destined for degradation is brought by vesicular transport to early endosomes, which mature into late endosomes and then fuse with lysosomes. During endolysosomal maturation the compartments change in morphology, cargo composition, position and intraluminal acidity in a tightly controlled manner.^{23–29} The most widely used manner to indicate distinct endolysosomal intermediates is their classification into “early endosomes (EE),” “late endosomes (LE)” and lysosomes (LY) (or variations hereon using other names).³⁰ However, these 3 categories are too limited in discriminating power when it comes to describing the dynamic continuum of interacting endolysosomal compartments or to indicate subpopulations of endolysosomes that differ by content, function, lysosomal activity, positioning or dynamics.^{31,32} Additional criteria are therefore required to be able to address fundamental yet still standing questions like: do all lysosomes carry out similar functions? How are lysosomal positioning and dynamics linked to endolysosomal maturation and functioning?

In our studies, we label endolysosomes by both genetically expressed LAMP-1-GFP³³ and endocytosed fluorescent dextran. LAMP-1 is a well characterized integral membrane protein that in steady state is mostly confined to the limiting membrane of late endosomes and lysosomes.²⁴ However, since newly synthesized LAMP-1 can travel to the plasma membrane for subsequent endocytosis, low levels can be found in early endosomes, as shown in previous immuno-EM studies.^{34,35} Moreover, since late endosomes and lysosomes fuse with autophagosomes, LAMP-1 is also present in autolysosomes. An overview of compartments that can contain LAMP-1 is given in Figure 1. Fluorescent dextran is a fluid phase endocytic tracer, which predominantly labels the degradative pathway.³⁶ Thus, constitutively endocytosed dextran will mark early and late endosomes, lysosomes and autolysosomes. Consequently, the identity of the LAMP-1-GFP- and/or dextran-positive compartments cannot be deduced from fluorescent images alone, but requires ultrastructural characterization. The main distinguishing morphological characteristics of endolysosomal compartments are described in numerous papers (reviewed in References 25,26; summarized in table 2 of Reference 24) and described in Table 1 of this paper.

A schematic overview of our live cell to 3D FIB-SEM CLEM procedure is given in Figure 2. We start our approach by culturing cells on gridded glass coverslips,⁴ which are etched with marks that are visible by both light microscopy and FIB-SEM (by imprinting the pattern in the Epon), allowing a first, coarse correlation between the 2 microscopes. The coverslips were coated with a circa 20 nm layer

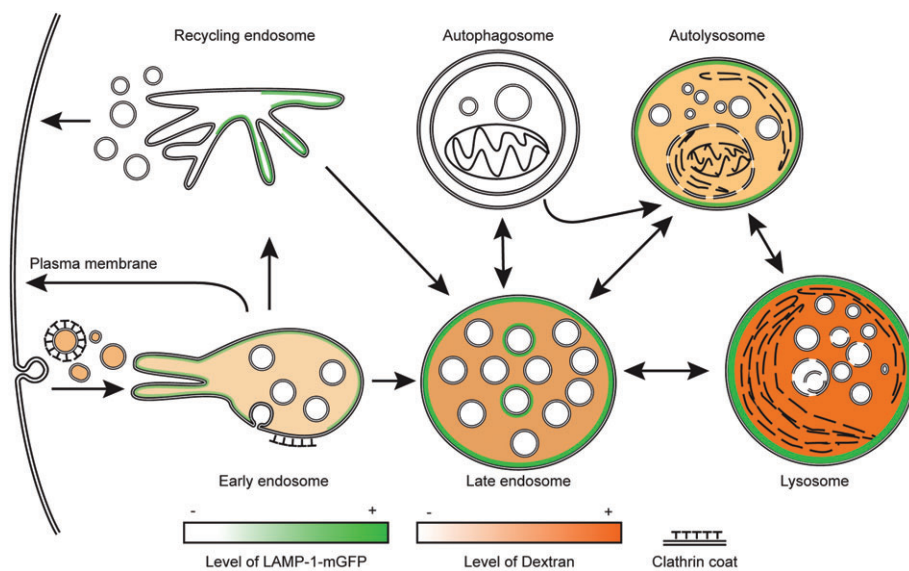


FIGURE 1 Schematic representation of the endolysosomal system showing the location of internalized fluorescent dextran (orange) and LAMP-1-GFP (green) and the morphological characteristics of different types of endolysosomal compartments. Arrows indicate sites of interactions between compartments, either via compartment fusion or vesicular transport

TABLE 1 Ultrastructural characteristics of endolysosomal compartments

Organelle type	Defining characteristics	References
Early endosome	Irregular shaped vacuole (100-500 nm) with electron-lucent lumen, often one or multiple tubular extensions. Loosely packed ILVs. Patches of bilayered clathrin lattices on limiting membrane.	27,37-41
Recycling endosome	Tubulo-vesicular membranes (60-100 nm diameter), with no discernable interior material. Clathrin-coated membrane buds can occur on tubules.	34,42-44
Late endosome	Irregularly shaped to globular shaped vacuole (250-1000 nm), sometimes with short tubular extensions. Densely packed with ILVs.	25,29,45-48
Lysosome	Highly variable, heterogeneous-shaped vacuole (200 to >1000 nm). Electron-dense lumen or irregular or amorphous content. Characteristic membrane whorls.	25,49-51
Autolysosome	Large, irregularly shaped vacuole (300 nm to >2000 nm), with highly heterogeneous content, electron-lucent and electron-dense regions, sometimes with remnants of degraded organelles and cytosolic material.	52-55

of carbon for easy removal of the coverslip once the cells were embedded in resin. HeLa cells were grown overnight on the carbon layer and transfected for LAMP-1-GFP for 5 hours. Then, the transfection medium was replaced with medium containing fluorescent dextran for 30 minutes at 37°C, followed by 2 hours at 20°C to block Golgi exit of newly synthesized GFP-tagged LAMP-1.^{35,56} Since under these conditions the newly synthesized LAMP-1-GFP only starts exiting the endoplasmic reticulum (ER), and has not yet reached the endolysosomal compartments, the 20°C block induces an accumulation of LAMP-1-GFP in the Golgi against an overall dark background of the cell. This facilitates the tracking of individual LAMP-1-GFP spots after releasing the block by placing cells at 37°C. We placed cells at 37°C 15 minutes prior to the start of live imaging, since this was the optimal period for warming up and create maximal visibility of post-Golgi LAMP-1-GFP-positive compartments. During live-cell imaging (Figure 2A), we only recorded the GFP channel, in a single focal plane, to reach the temporal resolution required to visualize transient trafficking events on a scale of seconds to tens-of-seconds (<500 ms between frames). We fixed cells in situ by adding double concentrated fixative directly to the medium in the live-cell holder, while the camera was still acquiring images. This prevented an imaging gap between the last live-cell frame and the fixed material. Movies were analyzed for regions of interest (ROIs) showing LAMP-1-GFP structures with distinct dynamic behaviors, such as movement,

fusion or interaction with other compartments. In the fixed material, Z-stacks of the ROI were recorded to visualize LAMP-1-GFP and in addition fluorescent dextran (Figure 2B). The area surrounding the ROI was imaged with both fluorescence and polarized light to map the location of cells in relation to the grid pattern (Figure 2C).

After completion of the steps described above, samples were postfixed in half-strength Karnovsky's fixative and stored in 1% formaldehyde or immediately taken for further processing. We applied 2 different postfixation strategies, either osmium tetroxide (OsO₄) followed by tannic acid and uranyl acetate (staining applied in Figure 3), or a heavier staining strategy using reduced osmium tetroxide-thiocarbohydrazide-osmium tetroxide (R-OTO) followed by uranyl acetate and Walton's lead aspartate (staining applied in Figures 4-6).^{57,58} Both protocols are described in-depth in Section 4. The latter strategy yielded more pronounced membranes and an overall better visualization of morphological details. After resin embedding and polymerization of the resin, the Epon block containing the imaged cell was separated from the coverslip by repeatedly dipping in liquid nitrogen and separating the glass from the resin surface with a clean razor blade. The pattern of the gridded coverslip on the resin surface (Figure 2D) greatly facilitated retracing of the ROI in the FIB-SEM.

The resin blocks were mounted on standard specimen stubs for SEM with the basal side of the cells facing up, rendered conductive

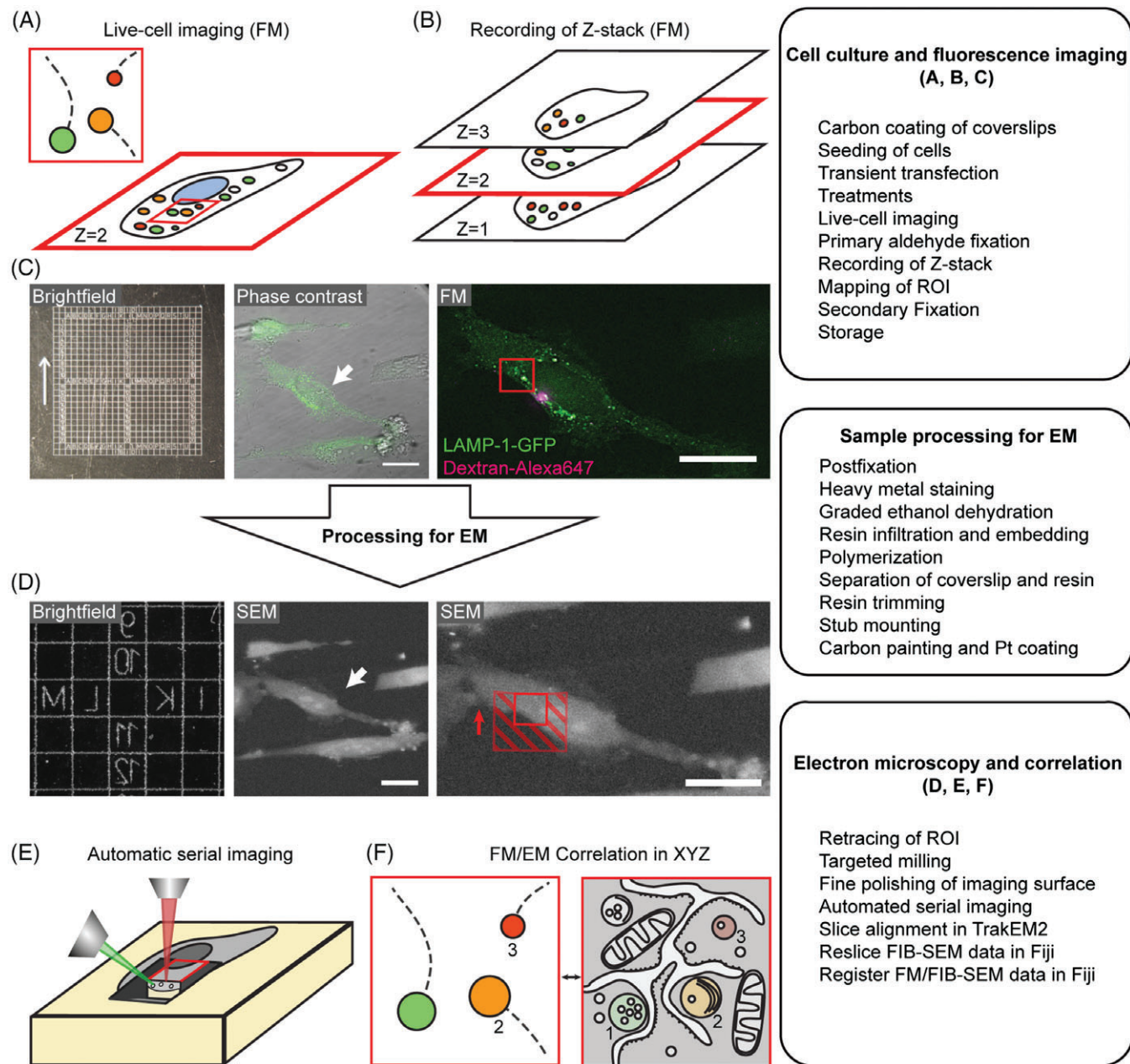


FIGURE 2 Schematic of the live-cell fluorescence to FIB-SEM workflow. A, LAMP-1-GFP transfected cells were incubated with dextran and after a 20°C block imaged live for several minutes, followed by in situ fixation. B, Z-stacks are recorded to define the focal plane of live imaging. C, Coordinates etched on gridded coverslips enable the retracing of cells after resin embedding. Coordinates of live-imaged cells (middle panel, white arrow) are registered using phase contrast after fixation, and ROIs for FIB-SEM imaging are determined based on live-cell data (right panel, red square). D, Retracing of live-imaged cells and targeting of ROIs is achieved through the imprinted coordinates of the gridded coverslips. Live-imaged cells are retraced in SEM using the imprinted coordinates after the glass coverslip is removed (middle panel, white arrow), followed by targeted milling of excess material around the ROI (right panel, ROI indicated in red, excess material indicated in striped red). Milling and imaging direction are indicated by red arrow). The middle and right panels are horizontally flipped to show the matching orientation with the FM images. E, Automated imaging is performed by repeatedly milling and imaging the ROI. F, Acquired FIB-SEM data sets are aligned and correlated to live-cell data and Z-stack

by carbon paint and platinum sputter coating, and transferred to the FIB-SEM. We found that the contours of the cells on the resin surface can be visualized by the backscattered electron (BSE) detector and that these contours closely match the cell shape imaged by brightfield microscopy (Figure 2D). By comparing the contours seen in SEM with the original live-cell imaging data, we could locate the ROI containing the previously live-imaged GFP-positive

compartments. This allowed us to target relatively small regions for volume imaging (Figure 2D,E), reducing the time required to image the ROI, while insuring that the volume EM data contained all live-imaged organelles (Figure 2F). We performed automated serial imaging either using a FEI Scios (Thermo Scientific; Figures 2–4) or a FEI Helios G3 UC (Thermo Scientific; Figure 5), which provides higher electron beam resolution. This is primarily advantageous to resolve

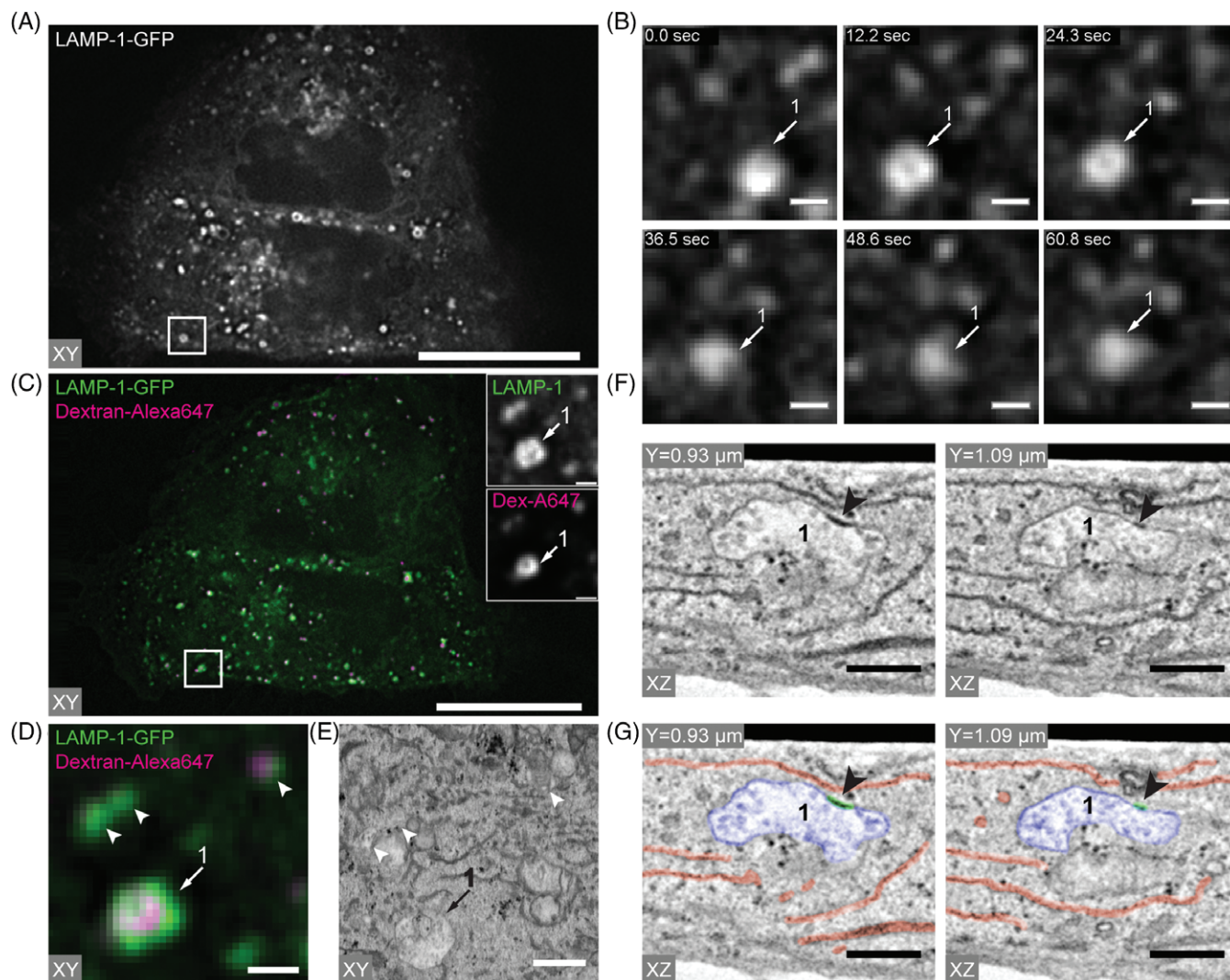


FIGURE 3 Live-cell CLEM of an early endosome. A, Still from Movie S1 at the start of live-cell imaging, showing the distribution of LAMP-1-GFP spots throughout the cell. The ROI selected for FIB-SEM, containing spot 1, is highlighted (white square). B, Magnified stills of the ROI (area in white square in A) showing LAMP-1-GFP-positive spot 1 at distinct time points. C, Slice from Z-stack after fixation showing the imaging plane with the ROI (white square). Insets: Enlargement of the ROI showing spot 1 in the GFP and dextran channels. D, Enlarged fluorescent image of the ROI shown in the white squares in A and C (white squares) and containing spot 1 to a size that corresponds to the FIB-SEM image as shown in E. Arrowheads indicate LAMP-1-GFP spots that were not tracked live, but could be correlated to the FIB-SEM data set as shown in E. E, FIB-SEM reconstruction of the ROI containing spot 1 in the same orientation as the FM image as shown in D. Arrowheads indicate endolysosomal compartments that could be correlated to the FM data shown in D. F, Individual slices from the FIB-SEM data set showing morphological characteristics of spot 1. Arrowheads point to the presence of a clathrin coat. G, Same image as in F, colored to highlight spot 1 (early endosome) (blue), ER (red) and clathrin coat (green). Movie S2 shows all FIB-SEM slices through the entire ROI, zooming in on spot 1 and providing a reconstruction of the 3D structure of spot 1, including the dissection of intraluminal vesicles and clathrin coat. Table 3 shows the collection of parameters gathered on spot 1. Scale bars for A, C: 25 μm ; B, D, E: 1 μm ; F,G:500 nm

small morphological characteristics and structures where distinct membranes are in close proximity, such as membrane contact sites (Figure 6). The imaging settings of all data sets are summarized in Table 2.

After automated imaging, we reconstructed the data set in the same orientation as our live-cell movies to compare the volume EM data to the fluorescence Z-stack. We retraced the focal plane of live-cell imaging by selecting at least 3 fluorescent spots from the live-cell imaging plane and measured the distances between the centers of these spots using Fiji. The pattern formed by these spots was then retraced in the volume EM data to identify the slice containing the previously live-imaged organelles (Figure S1). Thus, we used

individual compartments as landmarks for correlation between FM and FIB-SEM. When the Z-plane of live imaging was retraced in the FIB-SEM data set, we correlated all live-imaged compartments for ultrastructural analysis.

2.2 | Live-cell CLEM of a LAMP-1-GFP-positive early endosome

After establishing the optimized CLEM protocol for live-cell 3D CLEM (Figure 2), we performed a series of experiments on ROIs containing distinct LAMP-1-GFP-positive compartments that were visible for the duration of the movie and showed distinctive dynamic behaviors. In

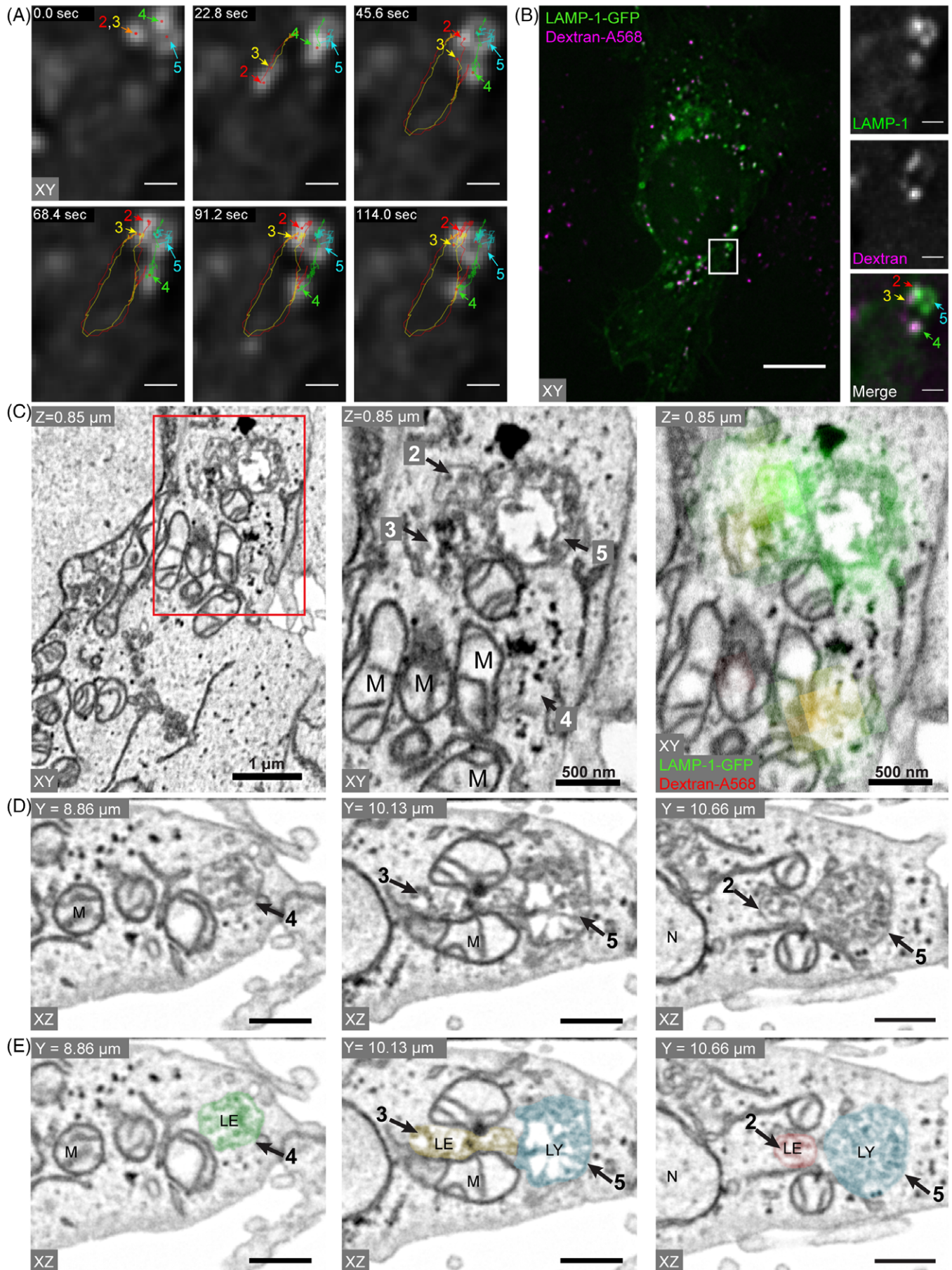


FIGURE 4 Legend on next page.

Figure 3A, we identify a dense LAMP-1-GFP spot with a dark core (further indicated as spot 1 in Figure 3A and Movie S1). This staining pattern is typical for LAMP-1, which is mostly present in the limiting membrane of endolysosomal compartments (Figure 1). The dense fluorescence represents LAMP-1-GFP in the limiting membrane, while the dark core represents the lumen that is devoid of LAMP-1-GFP. During live imaging, spot 1 was motile but within a restricted area, it remained within 2 μm from the plasma membrane (Figure 3B, Table 3).

The Z-stack after fixation revealed that the central compartment of spot 1 contained dextran, indicating that it was reached by internalized cargo (Figure 3C,D). After resin embedding, we retraced the cell and position of the ROI in the FIB-SEM (Figure 3E, Movie S2) and identified spot 1 as an irregularly shaped compartment measuring 1.28 μm in X, 0.8 μm in Y and 1.28 μm in Z, with an electron-lucent lumen containing intraluminal vesicles (ILVs) (Figure 3F). Using segmentation, we identified 45 ILVs. Moreover, part of the limiting membrane of the compartment was decorated with a clathrin coat, which covered a typical indentation of the vacuolar membrane³⁷ (Figure 3G, arrowheads, Movie S2). Clathrin coats on the limiting membrane of early, and to a lesser extent late endosomes contain concentrated cargo for sorting into ILVs, which depends on the endosomal sorting complexes required for transport (ESCRT).^{45,59,60} The irregular shape of the central vacuole, the electron-lucent lumen with loosely packaged ILVs and the presence of a clathrin coat define spot 1 as early endosome (Figure 1).

Combined, these live cell and EM data show a LAMP-1-GFP-positive early endosome, which displays diffusive movement in a restricted area near the plasma membrane. The presence of LAMP-1 in early endosomes may seem atypical since LAMPs are established markers of late endosomes and lysosomes. However, LAMPs can exit the TGN via the secretory pathway and travel via the plasma membrane and early endosomes to lysosomes,⁶¹ thus temporarily residing in early endosomes. Our data are also in line with previous immuno-EM studies showing the presence of endogenous LAMP-1 in early endosomes.³⁴

2.3 | Live-cell CLEM of late endosome-lysosome interactions

Next, we analyzed 4 LAMP-1-GFP-positive organelles over a period of 2 minutes (Figure 4A). For clarity, we use a continuous numbering of the imaged compartments throughout our figures (summarized in Table 3), which is why we refer to these spots as spot 2-5. Based on their morphology, we discriminated 3 condensed LAMP-1-GFP-

positive dots (spots 2-4) and a larger (approximately 0.8 μm) ring-shaped structure (spot 5) (Movie S3). These larger-sized ring structures were regularly observed and are characteristic for LAMP-1-GFP expressing cells.

Spots 2-4 were highly motile, and moved closely around the ring-shaped spot 5, which displayed a more stationary position (Table 3). In the first 30 seconds of imaging, spot 4 was so close to spot 5 that they could not be discerned by fluorescence microscopy (Figure 4A). Spots 2 and 3 initially moved freely, but after 60 seconds associated with spot 5 until fixation 1 minute later. Interestingly, we could still identify local spots of intense GFP signal on spot 5, indicating that spots 2 and 3 moved along with spot 5 for 60 seconds, while retaining their identities. After fixation, we found that spots 2-4 were all positive for dextran (Figure 4B), while the ring-shaped spot 5 was negative.

The FIB-SEM data revealed that spots 2, 3 and 4 have a very similar morphology (Table 3, Figure 4C). The 3 compartments were small (diameters between 0.3 and 0.5 μm) and irregularly shaped. Their lumens contained both electron-lucent and electron-dense regions, the latter indicating the presence of degraded material. Furthermore, the spots contained between 12 and 32 ILVs that occupied most of the volume of the compartment, resulting in tightly filled compartments (Figure 4D,E). Unlike the EE shown in Figure 3, spots 2-4 lacked a clathrin coat. Together, these characteristics identify spots 2-4 as late endosomes. Spot 5, which in live-cell imaging showed very different dynamics as spots 2-4, appeared in the FIB-SEM as a relatively large (0.77 \times 0.95 \times 0.95 μm), irregularly formed vacuole with both electron-lucent and electron-dense content, approximately 50 ILVs, and a large electron-lucent region (Figure 4D, middle and right panel, Figure 4E). This morphology is characteristic for lysosomes and autolysosomes, which both can appear as large vacuoles with irregular content (Table 1). Interestingly, we found late endosomal spots 2 and 3 closely opposed to the limiting membrane of (auto)lysosomal spot 5, but without membrane fusion profiles, neither between the 2 late endosomal spots 2 and 3 nor between late endosomes 2 and 3 and (auto)lysosome spot 5. This is consistent with the live-cell imaging observation that the fluorescence of spots 2 and 3 shows coordinated movement with spot 5, while remaining visible as distinct entities. Combined, our data indicates that (auto)lysosomes can be contacted by multiple late endosomes, which move together over prolonged periods of time without fusion.

FIGURE 4 Live-cell CLEM of multiple organelles in one sample. A, Stills from Movie S3 showing the tracks of 4 LAMP-1-GFP spots (spots 2-5) during 114 seconds of imaging. Spots 2 and 3 are highly dynamic and move back and forward to spot 5. Spot 4 moves away from spot 5 to remain stationary over a period of 60 seconds. Spot 5 is mainly stationary, and shows a typical appearance of LAMP-1-GFP-positive ring surrounding a dark lumen. B, Slice from Z-stack after fixation showing the overall distribution of both LAMP-1-GFP (green) and dextran-A568 (magenta) in the cell. Inset: Enlargement of the ROI displayed in A showing the presence of dextran (magenta) in spots 2-4 but not spot 5. (C) Slice from the reconstructed FIB-SEM data set in same orientation as the LM images in A and B. The left panel shows the location of spots 2 to 5 (indicated by the red rectangle) present in the ROI shown in A. The middle and right panels show an enlargement of the ROI indicated with the red rectangle in the left panel. In the right panel, the fluorescence labeling is overlaid on the EM structure using the same color coding as in A. D, Representative FIB-SEM slices of spots 2 to 5. E, Same images as in D, colored to highlight the shape of the correlated spots. Movie S3 shows all steps from live-cell imaging to the reconstruction of the 3D structure of spots 2 to 5 by FIB-SEM. Based on ultrastructural characteristics spots 2 to 4 are identified as late endosomes and spot 5 as (auto)lysosome. Table 3 shows the collection of parameters gathered on spots 2 to 5. Scale bars: A, B (cutouts), C (left panel): 1 μm ; B (full image): 10 μm ; C (middle and right panels) D, E: 500 nm

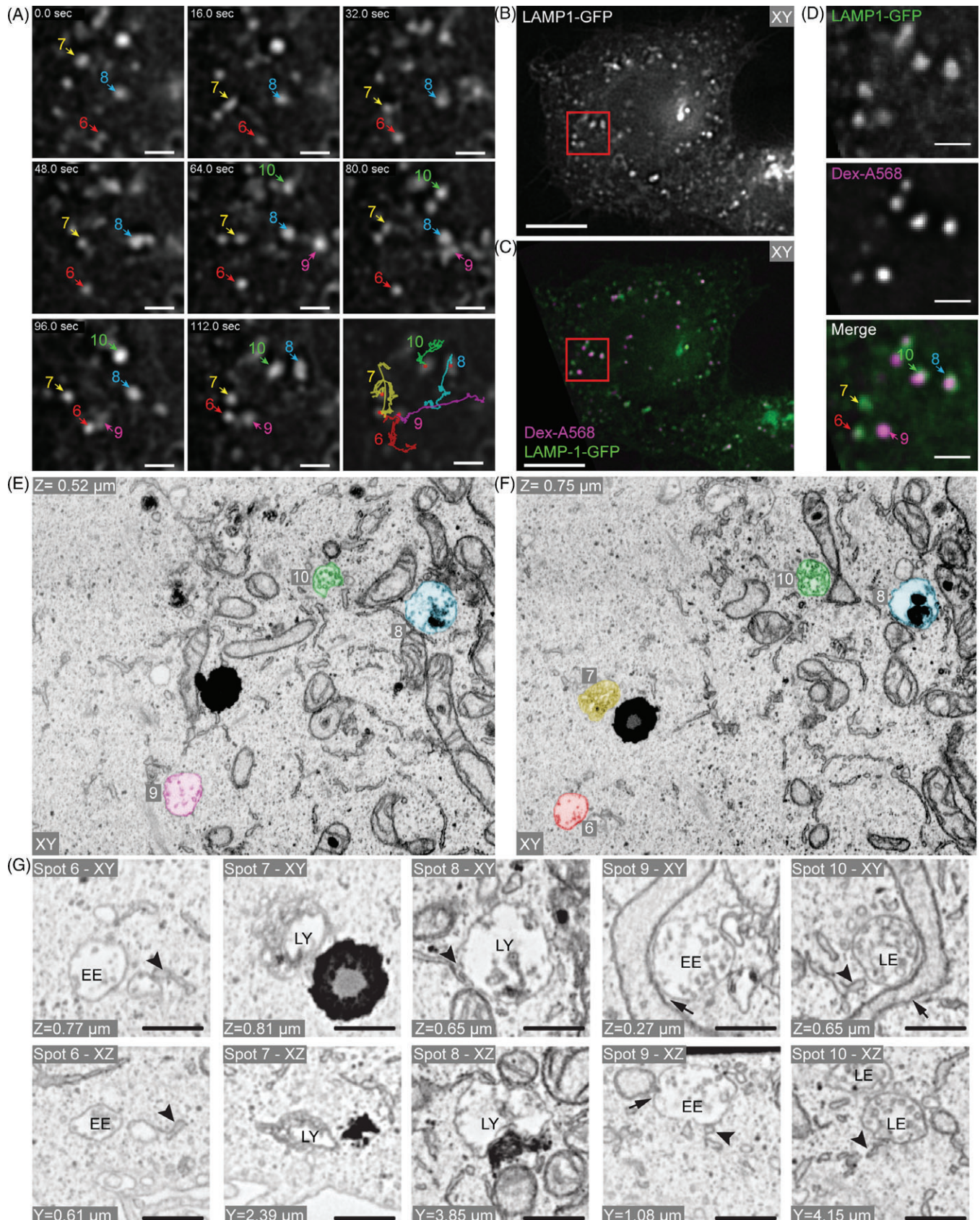


FIGURE 5 Legend on next page.

2.4 | Live-cell CLEM visualizing the ultrastructural context of endolysosomal compartments

In our next experiment, we focused on 5 highly motile LAMP1-GFP-positive spots (spots 6-10, Figure 5A,B). These spots exhibited

different movement patterns, either moving diffusely at low speed (spots 6 and 10) or showing stop-and-go movement,^{62,63} that is, bursts of movement followed by a period of no or slow movement (Movie S4, spots 7, 8 and 9). At 80 seconds, spot 7 interacted with a

nearby GFP-positive spot over a period of 10 seconds, after which these 2 spots could no longer be discerned, indicating a fusion event. At circa 96 seconds, spot 10 merged with a nearby fluorescent spot leading to an increase in local fluorescence intensity. Spot 9 became visible only later in the movie, at 64 seconds (Movie S4).

After fixation, we found that spots 8, 9 and 10 contained high levels of dextran, whereas spots 6 and 7 were only mildly positive (Figure 5C,D). In the fluorescent Z-stack, spots 9 and 10 were present in several 200 nm slices above and below the live-cell imaging plane, suggesting a large size for these compartments, or, alternatively, the presence of multiple compartments located on top of each other. The live-cell data on spots 6 to 10 are further summarized in Table 3.

In the FIB-SEM data, we retraced spots 6 to 10 as morphologically diverse structures (Figure 5E,F). Spot 6 appeared as an irregularly shaped compartment, measuring 0.55 μm in X, 0.41 μm in Y and 0.54 μm in Z. The lumen of spot 6 was mostly electron lucent with approximately 25 ILVs (Figure 5G). These characteristics identify spot 6 as an early endosome (Table 3). Interestingly, these data show that early endosomes do not always contain a clathrin coat during maturation. This type of information is difficult to extract from 2-dimensional (2D) EM data, since clathrin coats cover only limited areas of the endosomal vacuole, which in 2D EM may be present outside the section. The presence of a clathrin coat is probably dependent on cargo supply.

Spot 7 was identified as an irregularly shaped compartment measuring 0.55 μm in X, 0.41 μm in Y and 0.54 μm in Z, containing approximately 50 ILVs and small regions of electron-dense material, as well as a large electron-lucent region (Figure 5G). Based on these typical morphological characteristics we classified spot 7 as lysosome or autolysosome. Interestingly, while its morphology is very similar to (auto)lysosomal spot 5 from Figure 3, the dynamics of spot 7 are vastly different. Spot 5 was mostly immotile, whereas spot 7 traveled relatively fast over a large distance. This shows that individual lysosomes/autolysosomes can display variable dynamic behavior. Further studies using multiple marker proteins are required to define whether these dynamic differences represent different lysosomal subpopulations.

Spot 8 appeared as a spherical compartment measuring 0.83 μm in X, 0.76 μm in Y and 0.90 μm in Z. The lumen of spot 8 contained an electron-lucent region with approximately 60 scattered ILVs, as well as an electron-dense region containing membrane whorls (Figure 5G). This identified spot 8 as a lysosome. Spot 9 appeared as

a large, spherical compartment measuring 0.71 μm in X, 0.61 μm in Y and 0.74 μm in Z. Its lumen was packed with approximately 100 ILVs, of different sizes (Figure 5G). This identified spot 9 as an intermediate stage between early and late endosome. Finally, at spot 10, we found 2 irregularly shaped compartments in close proximity to each other. Both compartments were similar in size (0.49 μm in X, 0.5 μm in Y and 0.60 μm in Z vs 0.69 μm in X, 0.6 μm in Y and 0.49 μm in Z) and morphology, with an electron-lucent lumen densely filled with ILVs (Figure 5G). We classified both spots as late endosomes. Thus, spot 10 did not represent one compartment but consisted of 2 late endosomes. By live-cell imaging, we observed an increase in fluorescence of spot 10 at circa 96 seconds, indicative of a fusion event. In the FIB-SEM, however, we observed no membrane fusion profile between the 2 late endosomes identified as spot 10. These data indicate that a local increase in fluorescence observed by diffraction-limited live-cell imaging can either represent a fusion event or the close proximity of 2 compartments, which move closely together and cannot be discerned as individual compartments.

2.5 | Live-cell CLEM reveals multiple contact sites between LAMP-1-GFP-positive compartments and ER

An important feature of volume EM data as obtained with FIB-SEM is that the correlated fluorescent compartment is visualized in 3D, amidst other, nonfluorescent subcellular structures. In case of endolysosomal compartments, interactions with ER through membrane contact sites can affect their identity and mobility.⁶⁴⁻⁶⁷ Membrane contact sites are defined as regions where organelle membranes are closely apposed (<30 nm), but not fusing.⁶⁸⁻⁷⁰ The limited thickness of a TEM section prevents efficient studies of membrane contact sites, since only parts of an organelle are visible in a given section. Previous work has demonstrated the feasibility of FIB-SEM to resolve membrane contact sites in 3D.⁷¹ Here, we analyzed our data sets for the presence of contact sites between correlated endolysosomal compartments and the ER.

Our FIB-SEM data showed that ER membranes are found in abundance within 30 nm of the limiting membrane of endolysosomal compartments. The ER cisternae often follow the limiting membrane of the endolysosomal organelles, conforming to their shapes (Figure 6C,D, Movie S4). In addition, we regularly found that the tip of an ER cisterna closely apposed the endolysosomal organelle. Remarkably, these contact sites were observed regardless of

FIGURE 5 Live-cell CLEM provides context information to dynamic endolysosomal compartments. A, Stills from Movie S4 showing the tracks of 5 LAMP-1-GFP spots (spots 6-10) during 112 seconds of imaging. Spots 7 to 9 exhibit typical stop-and-go movement. The lower right panel shows the tracks of spots 6 to 10 overlaid over the final frame of live-cell imaging data before fixation. B, Still from Movie S4 showing the distribution of LAMP-1-GFP just prior to fixation. The ROI selected for FIB-SEM is indicated by the red square. C, Slice from the Z-stack after fixation showing the distribution of LAMP-1-GFP (green) and dextran (magenta). The ROI selected for FIB-SEM (shown in A) is indicated by the red square. D, Magnification of the ROI (imaged in A and indicated by the red squares in B and C) showing the distribution patterns of LAMP-1-GFP and dextran in spots 6 to 10. E, Pseudocolored virtual slice of the FIB-SEM reconstruction of the ROI showing spots 8, 9 and 10 in the same orientation as the FM images in A-C. (F) Pseudocolored virtual slice of the FIB-SEM reconstruction of the ROI, located 230 nm above slice shown in E, showing spots 6, 7, 8 and 10. G, Representative FIB-SEM slices of spots 6 to 10 in both XY and XZ orientation. Based on ultrastructural characteristics we made the following identifications: Spot 6 early endosome; spot 7 (auto)lysosome; spot 8 lysosome; spots 9 and 10 late endosomes. Contact sites with ER (arrowheads) and mitochondria (arrows) are indicated. Table 3 shows the collection of parameters gathered on spots 6 to 10. Scale bars: A, D: 2 μm ; B, C: 10 μm ; E, F: 1 μm ; G: 500 nm

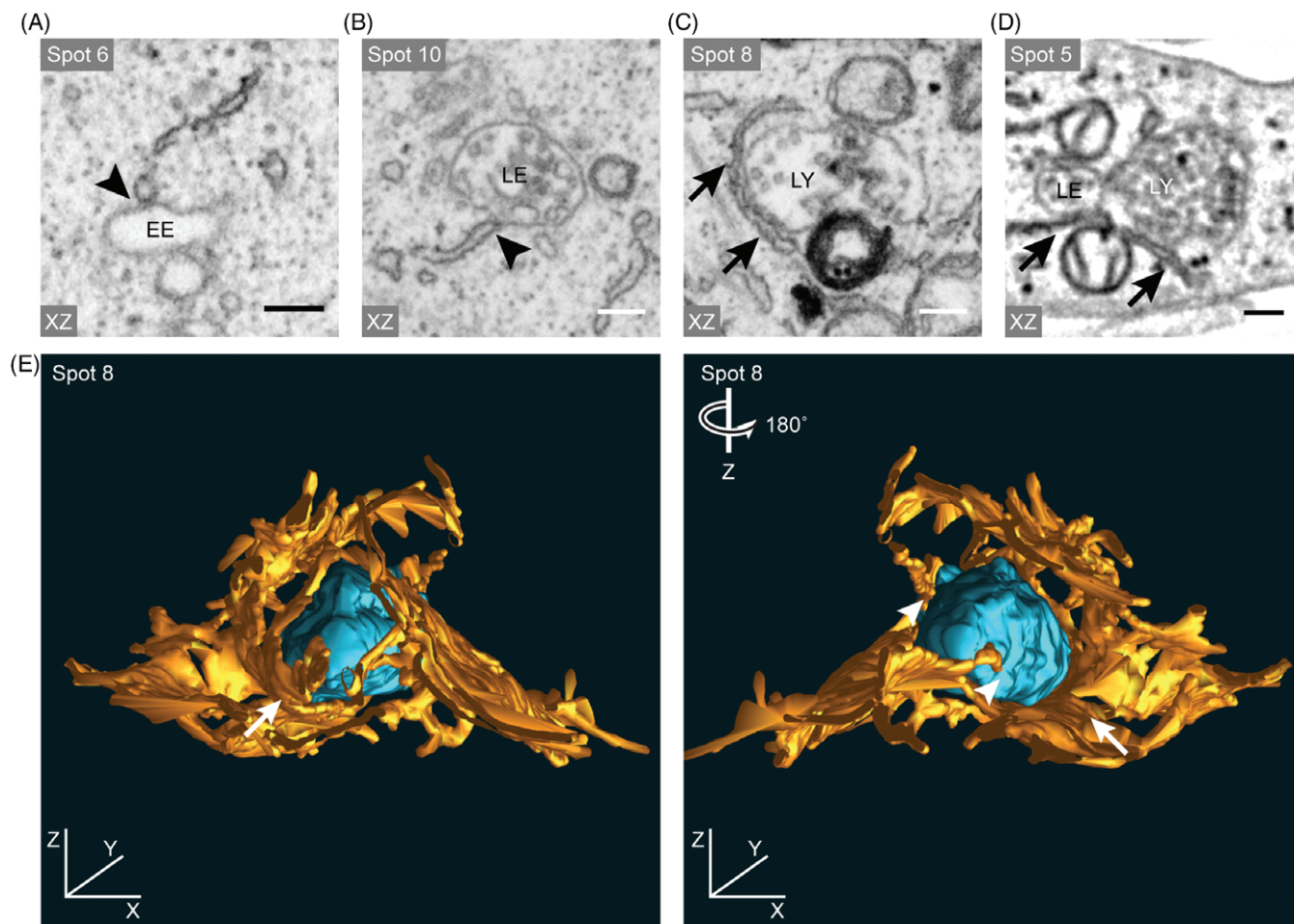


FIGURE 6 FIB-SEM visualizes ER contact sites with early and late endolysosomal compartments. A-D, FIB-SEM slices of spots 5, 6, 8 and 10 (same numbering as in Figure 5) in XZ direction, showing interactions with the ER. Arrowheads point to contact sites with tips of ER cisternae and arrows to contact sites with ER sheets. A, Contact site between early endosomal spot 6 and ER. B, Contact site between late endosomal spot 10 and ER. C, ER cisternae covering a substantial area of the limiting membrane of lysosomal spot 8. D, Contact site between (auto)lysosomal spot 5 and an ER sheet. E, Segmented 3D model of lysosomal spot 8 (cyan) together with the surrounding ER (orange). The multiple contacts sites between spot 8 and ER are indicated. Movie S4 shows all steps from live-cell imaging to the reconstruction of the 3D structure of spots 6 to 10 by FIB-SEM, and shows the interaction of spot 8 with the ER

organelle type (Figure 6A-D, Table 3), and found associated with early endosomes, late endosomes and lysosomes/autolysosomes. The majority of the live-imaged spots had at least one contact site with the ER, while several spots showed multiple contact sites at distinct locations on the compartment (Table 3, Figure 6E). These data show that ER forms contact sites occur in abundance with multiple types of endolysosomal compartments, and that FIB-SEM provides a powerful tool to study these interactions in 3D.

3 | DISCUSSION

We present an efficient method to routinely trace individual compartments from live-cell fluorescence all the way to volume EM, a method we refer to as single organelle microscopy. The high spatio-temporal resolution of our method maximizes the number of dynamic and ultrastructural parameters that within one experiment can be integrated onto a single organelle, in 3D. The relatively high

TABLE 2 Image acquisition parameters of 3D data sets

	Figure 3	Figure 4	Figure 5
Microscope	FEI Scios	FEI Scios	FEI Helios G3 UC
Acceleration voltage (kV)	2	2	2
Beam current (nA)	0,2	0,2	0,2
Pixel dwell time (μ s)	15	10	10
Lateral pixel size (nm)	6	5	5
Slice thickness (nm)	10	10	5
Slices	1065	1120	1176
Volume of data set (XYZ μ m)	14.8 \times 4.6 \times 10.6	17.7 \times 5.9 \times 11.2	15.4 \times 4.2 \times 5.8

TABLE 3 Overview of dynamic and morphological characteristics of individual correlated spots

Spot No.	Average speed ($\mu\text{m/s}$)	Peak speed ($\mu\text{m/s}$)	Displacement in 110 s (μm)	Movement ^a	Fusion events at timepoint ^b	Dextran	Size (by FIB-SEM) (μm)	No of ILVs	Morphological hallmarks	Organelle type	ER contact sites ^c
1	0.2	0.739	1.815	Diffusive	-	+	X: 1.28 Y: 0.80 Z: 1.28	45	Irregularly shaped vacuole. Electron-lucent lumen, loosely packed ILVs. Clathrin patch on limiting membrane.	Early endosome	7
2	0.152	0.975	3.350	Stop-and-go	-	+	X: 0.38 Y: 0.29 Z: 0.37	32	Mostly globular vacuole with electron-lucent and electron-dense content. Densely packed ILVs.	Late endosome	2
3	0.135	1.102	3.420	Stop-and-go	-	+	X: 0.62 Y: 0.43 Z: 0.53	22	Rounded to irregularly shaped vacuole with electron-dense content. Densely packed ILVs.	Late endosome	4
4	0.105	0.567	2.310	Diffusive	-	+	X: 0.53 Y: 0.46 Z: 0.54	12	Rounded vacuole with electron-dense content. Densely packed ILVs.	Late endosome	3
5	0.128	0.73	0.489	Diffusive	-	-	X: 0.77 Y: 0.95 Z: 0.83	45	Irregularly shaped vacuole with heterogeneous content, with electron-dense and electron-lucent material.	(Auto)lysosome	6
6	0.185	1.334	3.34	Diffusive	-	\pm	X: 0.55 Y: 0.41 Z: 0.54	25	Irregularly shaped vacuole. Electron lucent lumen with loosely packed ILVs.	Early endosome	1
7	0.251	2.034	2.098	Stop-and-go	87 s	\pm	X: 0.55 Y: 0.41 Z: 0.54	50	Irregularly shaped vacuole. Heterogeneous content containing electron-dense and electron-lucent regions.	(Auto)lysosome	0
8	0.159	1.172	3.323	Stop-and-go	-	+	X: 0.83 Y: 0.76 Z: 0.90	60	Irregularly shaped vacuole. Contains heterogeneous ILVs, amorphous material and electron-dense membrane whorls.	Lysosome	4
9	0.204	0.904	5.692 ^d	Stop-and-go	-	+	X: 0.71 Y: 0.61 Z: 0.74	100	Irregularly shaped to rounded vacuole with electron-lucent lumen. Many ILVs but loosely packed.	Early/late endosome	5
10	0.197	0.69	1.977 ^d	Diffusive	92.8 s	+	X: 0.49 Y: 0.50 Z: 0.60	70	Two separate compartments without fusion profile. Both are globular vacuoles containing densely packed ILVs.	Two late endosomes	2

^a Movement is either scored as diffusive (random, nondirectional movement) or stop-and-go (alternating periods of fast, directional movement and slow, nondirectional movement).

^b Fusion events are scored when individual LAMP-1-GFP(+) spots become indiscernible.

^c ER contact sites were scored when ER membranes were within 30 nm of limiting membrane of endolysosomal compartment.

^d Spots 9 and 10 were only followed for 58 and 50 s, respectively.

throughput of the pipeline allows for quantitative measurements on dynamic behavior and ultrastructural characteristics. Using this method, we provide the proof of principle to directly link dynamic information on the behavior of individual endolysosomes to their ultrastructural characteristics in 3D.

Previously, correlative live-cell imaging and volume EM approaches were mainly used to identify a rare or transient structure or event,^{1,2,7,20,31} without taking into account the intracellular trafficking steps leading to this event. Here, we present a cohesive experimental pipeline that integrates key temporal and structural parameters, that is, live-cell dynamics, architecture and cellular context, on a single organelle over an extended period of time. By live-cell imaging we monitor the dynamic local behavior of individual organelles during several minutes prior to fixation. This allows us to define transient interactions, movement patterns and subcellular positioning, which are important factors to determine the identity and function of endolysosomal compartments, and can only be studied in live cells. The resolution of EM is required to establish compartment identity, visualize fusion profiles with other compartments, show interactions with surrounding membrane and nonmembrane structures, and to provide unique information on the intra-organelle membrane organization. This is illustrated by the collection of spots in Table 3, which clearly shows that the presence of LAMP-1-GFP or dextran alone cannot establish organelle identity. The FIB-SEM has the resolution to capture high-resolution ultrastructural information in 3D, visualizing local ultrastructural details, such as clathrin coats, membrane whorls and ILVs. Vice versa, by using live-cell imaging we can select small, well-defined ROIs for FIB-SEM imaging, which ensures that the organelles of interest are embedded within the final 3D data sets. This selection of small ROIs through fluorescence combined with the precise, targeted removal of excess material using the gallium beam reduces FIB-SEM imaging and data processing time, increasing the overall throughput of the workflow. Of note, of the 10 LAMP-1-GFP spots analyzed in this paper (selected based on their visibility in the live-cell movie), only 3 meet the morphological criteria of a lysosome. Since LAMP-1-GFP in numerous studies is referred to as an established marker for late endosomes-lysosomes,^{23,33,72} or even strictly lysosomes,^{73,74} these data illustrate that defining organelle identity by FM, using overexpressed proteins, may lead to incorrect interpretations.

By live-cell imaging we found that LAMP-1-GFP-positive compartments frequently interact with each other over extended periods of time. Volume EM proved essential to interpret the nature of these interactions. For example, in Figure 4 we show prolonged contact of late endosomal spots 2 and 3 with (auto)lysosomal spot 5 in live cells, but investigation by FIB-SEM showed no evidence for membrane fusion. A similar observation was made in Figure 5, where we found that spot 10 increased in brightness after interaction with another GFP-positive spot, forming a larger, brightly fluorescent compartment. By FIB-SEM we found that spot 10 consisted of 2 closely associated late endosomes which were not fused. Together, our data show that endolysosomal compartments can move together during prolonged periods without fusion. Although, we did not detect fusion of these compartments in our FIB-SEM data, this does not exclude the possibility of exchange of material between the tracked

organelles, as previous studies established a mechanism known as kiss-and-run, where endolysosomal organelles undergo transient fusion events, allowing the exchange of luminal content while retaining 2 distinct compartments.⁷⁵

In addition to visualizing the morphology of endolysosomal compartments, volume EM also visualizes all structures surrounding the organelles, revealing compartments not detected by fluorescence microscopy. This is shown in Figure 6, where we show diverse LAMP-1-GFP-positive compartments in relation to the context of LAMP-1-GFP negative structures, such as ER and mitochondria. Interactions of endolysosomal compartments with ER at membrane contact sites are required for a range of processes, including signaling, transport of metabolites, endolysosomal transport and compartment maturation.^{64,65,68,69,76–78} Membrane contact sites are morphologically identified as closely apposed membranes (<30 nm), and molecularly by the presence of tethers,^{67,69,70} suggesting that EM is essential to study these domains in detail. In Figure 6, we demonstrate the feasibility of using FIB-SEM to determine the level of interaction between previously live-imaged endolysosomal compartments and ER (Table 3) in 3D, indicating volume EM provides sufficient resolution to examine the presence and structure of inter-organelle contacts.

In our studies, we performed chemical fixation *in situ* by adding fixative to the imaging chamber during imaging. While chemical fixation is considered as a slow process due to the limited penetration rate of glutaraldehyde and formaldehyde, we found that the relative position of compartments barely changed between the last frame of the live-cell movie and the fluorescent Z-stack recorded after fixation, indicating that chemical fixation is sufficiently fast for our application, and allowing us to link the dynamic information obtained by live-cell imaging to ultrastructure in 3D. Processing steps for EM are also known to introduce alterations in a sample, like shrinkage, which may affect the morphology of individual compartments.^{49,79–81} Interestingly, measurements on the distance between organelles in fluorescence and FIB-SEM revealed very limited changes in the XY direction (as shown in Figure S1). In Z, the distances of organelles relative to the coverslip were 300 to 400 nm shorter in FIB-SEM than would be expected from the FM data, which is within the axial resolution limit of FM (approximately 500 nm). For approaches that rely on serial sectioning, this could hamper the retracing of organelles between FM and EM. However, since FIB-SEM captures the full volume of the ROI rather than individual slices, this did not cause any pronounced difficulties in correlating the live-imaged compartments in Z. Thus, the collected FIB-SEM volume can rapidly be examined for the presence and relative positioning of the live-imaged organelles in the X, Y and Z-axis.

In the data presented here, we use LAMP-1-GFP and dextran for fluorescent imaging, but our method can be extended for all types of fluorescent probes, for example, to examine the functional state of organelles. Enzyme activity, the presence of ions and changes in pH are important determinants for endolysosomal function. Several fluorescent probes are available to examine these properties (LysoTracker, Magic Red Cathepsin substrates, calcium sensors), but the nature of these probes prevents imaging in fixed material, since fixation perturbs membrane integrity, inactivates enzymes and

neutralizes pH or ion gradients.^{31,82} With live-cell CLEM, functional information can be obtained in live cells and correlated to the underlying 3D ultrastructure. Furthermore, we can extend our method to include specialized FM approaches to study transient close-range interactions (fluorescence resonance energy transfer [FRET]) and compartment dynamics and membrane trafficking (FRAP). Use of super-resolution techniques would further increase the flexibility of the pipeline, providing more detailed information of subcellular structures with greater spatiotemporal resolution in live cells.⁸³ The increased lateral and axial resolution of super-resolution FM would provide not only more accurate fluorescence localization but would also serve to increase the registration accuracy between live imaging and volume EM.

It is becoming increasingly clear that endolysosomal trafficking, positioning and organelle interaction are important parameters for lysosomal maturation, membrane interactions and functioning.^{84,85} Moreover, defective regulation of endosomal trafficking is seen in many neurological disorders, like Huntington's disease, Alzheimer and Charcot-Marie-Tooth type 2B,^{72,86,87} and subpopulations of lysosomes are linked to axon formation and cancer progression.^{88,89} To be able to understand the function and regulation of these dynamic interactions it is required that ultrastructural and molecular characteristics are directly linked to parameters that can only be derived from live cells, such as organelle dynamics, positioning and enzyme activities. Since our approach integrates information on the dynamics, molecular composition and ultrastructural context of a single compartment, it is highly suited for multiparameter examination of individual organelles, in healthy and diseased states.

In conclusion, we present a flexible platform to combine available fluorescence microscopy approaches with 3D ultrastructural visualization that reliably links organelle dynamics and ultrastructure, a method we refer to as single organelle microscopy. In addition, we provide a method that allows the selection of ROIs for efficient and targeted FIB-SEM imaging.

4 | MATERIALS AND METHODS

4.1 | Cell culture and transfection

HeLa cells were cultured in a 37°C, 5% CO₂ incubator, in T75 culture bottles (Corning). Cells were maintained in Dulbecco's Modified Eagle's Medium (DMEM; Gibco) supplemented with 10% fetal bovine serum (FBS), 2 mM L-glutamin, 100 U/mL penicillin, 100 µg/mL streptomycin (referred to as completed DMEM). Cells were passaged when confluency reached 85% to 90%, and tested for mycoplasma infection every 4 weeks. Transfections were performed using Effectene transfection reagent (Qiagen) according to manufacturer's instructions.

For correlative live-cell imaging, we used 25 mm diameter photo-etched gridded coverslips (Ibidi GmbH). The coverslips were coated with 2 layers of carbon (total thickness 20 nm) to promote cell adhesion and improve their dissociation from Epon resin, using an Edwards 306 auto vacuum evaporator using thick carbon wire (Agar Scientific, AGE428). Following carbon coating, the coverslips were heated to 120°C overnight. The sterilized coverslips were transferred

to 6-well culture plates (Corning) and ultraviolet (UV) sterilized for at least 30 minutes, after which HeLa cells were seeded at a density of 1.5×10^5 cells/dish on day 1 under regular culture conditions. On day 2, cells were transiently transfected with a construct encoding LAMP1-GFP at 37°C for 5 hours, after which they were treated with 500 µg/mL dextran-Alexa conjugates (Alexa568 or Alexa 647, Life Technologies) in complete medium supplemented with 30 mM HEPES, to mark degradative compartments. Thirty minutes after dextran addition, cells were incubated at 20°C for 2 hours outside of an incubator to apply a Golgi exit block.

Prior to live-cell imaging, cells were washed 3 times with phenol-red-free DMEM supplemented with 2% FBS, 2 mM L-glutamin, 100 U/mL penicillin, 100 µg/mL streptomycin (referred to as live-imaging medium), to remove unbound dextran-Alexa conjugates. The coverslips were mounted in a live-cell imaging holder which was filled with 1 mL live-imaging medium.

4.2 | Live-cell imaging and in situ fixation

Live imaging was performed on a Deltavision RT widefield microscope (GE Healthcare) equipped with a conditioned imaging chamber set to 37°C and 5% CO₂. Time-lapse imaging was performed using a 100×/1.4 numerical aperture (NA) oil immersion objective and images were recorded on a Cascade II EM-CCD camera (Photometrics) with a gain value of 290 using the Acquire3D module in Softworx 6.5.2. An image of the GFP channel was recorded every 400 ms with an exposure time of 100 ms.

Cells were stabilized in the imaging chamber for 15 minutes prior to image acquisition, to recover from the Golgi exit block. Live-cell imaging was performed to track LAMP1-GFP labeled compartments for 2 minutes, after which the cells were fixed in situ by addition of 1 mL of fixative containing 4% paraformaldehyde (Sigma) and 0.05% glutaraldehyde (25% solution in dH₂O, Merck) in 1× PHEM buffer (60 mM PIPES, 25 mM HEPES, 10 mM EGTA, 2 mM MgCl₂, pH=6.9) to the imaging holder with the camera still active, to obtain images until the cells are fixed. After fixation, a Z-stack was recorded for all fluorophores. Using the etched pattern on the coverslip, the position and orientation of the imaged cell was recorded by phase contrast at a low magnification.

4.3 | Postfixation, dehydration and resin embedding

Following primary fixation, the coverslips were transferred to 35 mm dishes and postfixated in 2.5% glutaraldehyde and 2% paraformaldehyde in 0.1 M sodium cacodylate buffer (CB). Samples in Figures 2 and 3 were postfixated using 1% OsO₄ with 0.8% K₃Fe(III)(CN)₆ in 0.1 M CB for 1 hour on ice. Coverslips were washed 5 times in 0.1 M CB, and then treated with 1% tannic acid (Mallinckrodt Pharmaceuticals) in ddH₂O for 1 hour on ice. Samples were washed 5 times using ddH₂O and stained using 1% uranyl acetate in ddH₂O for 1 hour, in the dark at room temperature. After thorough rinsing using ddH₂O, the coverslips were passed through a graded ethanol: ddH₂O series for dehydration (50%, 70%, 90%, 96%, 100% for 2 × 5 minutes each, and 100% with acidified dimethoxypropane for 6 × 5 minutes). Samples were stepwise infiltrated with Epon resin

(25%, 50%, 75% in ethanol for 1 hour each), followed by 2 infiltration steps using 100% Epon resin, first for 1 hour, then 16 hours. Final embedding of the coverslips in 100% Epon resin was carried out in 35 mm dishes, and the resin was polymerized for 72 hours at 60°C.

For further improvement of electron contrast, the samples in Figures 4 and 5 were poststained with 1% OsO₄ with 1.5% K₄Fe(II)(CN)₆ in 0.065 M CB for 1 hour on ice. Coverslips were washed 6 times in ddH₂O, followed by treatment with 1% thiocarbonylhydrazide (Sigma) at 30°C for 15 minutes, after which the coverslips were washed 6 times in ddH₂O. The coverslips were then treated with 1% OsO₄ in ddH₂O on ice for 30 minutes followed by 6 washes in ddH₂O. The samples were then treated with 2% uranyl acetate in ddH₂O for 30 minutes in the dark, followed by 6 washes in ddH₂O. The samples were stained using Walton's lead aspartate (pH 5.6) for 30 minutes at 60°C.⁹⁰ Samples were washed twice with ddH₂O and subjected to a graded ethanol dehydration series and infiltrated with Epon resin in the way described above.

4.4 | Resin block processing and FIB-SEM tomography

After polymerization, excess material surrounding the carbon-coated part of the coverslip is removed using a small handsaw, resulting in a small slab of resin with the carbon-coated coverslip attached. The coverslip is removed from the resin surface by repeatedly dipping the sample in liquid nitrogen and dH₂O at room temperature, after which the glass was removed with a clean razor blade. The exposed surface was cleaned using dH₂O.

The resin-embedded cells are mounted on 12 mm aluminum stubs for SEM using carbon adhesive discs (Agar Scientific), and the sides of the resin block were covered with conductive carbon cement (Agar Scientific) to establish a conductive path to reduce charging effects. To further improve conductivity, the surface of the sample was coated with a 4 nm layer of Pt using a Cressington 208HR sputter coater. Samples were imaged with a Scios FIB-SEM (Figures 1–4) or a Helios G3 UC FIB-SEM (Figure 5) (Thermo Scientific) under high-vacuum conditions. The grid pattern embedded in the resin surface was used to retrace the cell of interest, after which the cell contour in SEM was compared with the fluorescence Z-stack to determine the ROI. Using the FIB, a 500 nm thick layer of Pt was deposited over the ROI, at an acceleration voltage of 30 kV and a current of 1 nA. Trenches flanking the ROI were milled at an acceleration voltage of 30 kV, using a high current (5–7 nA), followed by a staircase pattern in front of the ROI to expose the imaging surface. Fine polishing was performed with the ion beam set to 30 kV with a beam current of 0.5 nA, resulting in a smooth imaging surface. Serial imaging was then performed using the in-column backscattered electron detector (imaging settings per experiment are detailed in Table 2).

4.5 | Image processing

Widefield time-lapse series and Z-stacks were deconvolved using Softworx 6.5.2 (GE Healthcare). Manual tracking and annotation of organelles was performed using the MTrackJ plugin for Fiji.⁹¹

FIB-SEM images were imported as image stack in Fiji⁹² and aligned to each other using TrakEM2.⁹³ The aligned stack was rotated 90° along its X axis to visualize the FIB-SEM data in the same orientation as the fluorescence z-stack. The FIB-SEM data was manually correlated with the fluorescence data by using endolysosomal compartments as landmarks. This pattern of landmarks and the distances between them was used to register the positions of organelles between FM and EM images. Aligned stacks were also exported and converted to the MRC file format for use in IMOD⁹⁴ to perform manual segmentation, 3D modeling and movie generation. Movies were prepared and generated using Adobe Premiere Pro CC 2017 (Adobe Systems) and saved as .MP4 files with h.264 compression.

ACKNOWLEDGMENTS

We acknowledge C. de Heus and G. Posthuma for assistance with cell culture and specimen preparation and C.T.H. Schneijdenberg and S. Matveev for assistance with the FIB-SEM systems.

Conflict of interest

The authors declare no potential conflict of interests.

Financial disclosures

This work was supported by funding from Stichting voor de Technische Wetenschappen STW, grant number 12715, granted to Hans Gerritsen and Judith Klumperman.

Author contributions

J.K., J.F. and N.L. designed the study, analyzed the data and wrote the manuscript. J.F. carried out live-cell imaging and FIB-SEM data collection. C.t. B. provided technical support for live-cell imaging and fluorescence microscopy. E.G.v.D. and W.H.M. optimized and performed sample preparation. N.L.S. and Y.S. provided support for sample preparation, image processing and data analysis. H.C.G., W.H.M. and Y.S. reviewed the manuscript.

Editorial Process File:

The Editorial Process File is available in the online version of this article.

ORCID

Job FERMIE  <http://orcid.org/0000-0002-7340-0377>

REFERENCES

1. Karremans MA, Mercier L, Schieber NL, et al. Fast and precise targeting of single tumor cells in vivo by multimodal correlative microscopy. *J Cell Sci.* 2016;129(2):444-456.
2. Bushby AJ, Mariggi G, Armer HEJ, Collinson LM. Correlative Light and Volume Electron Microscopy: Using Focused Ion Beam Scanning Electron Microscopy to Image Transient Events in Model Organisms. *Methods Cell Biol.* 2012;111:357-382.
3. Van Rijnsoever C, Oorschot V, Klumperman J. Correlative light-electron microscopy (CLEM) combining live-cell imaging and immunolabeling of ultrathin cryosections. *Nat Methods.* 2008;5(11):973-980.

4. Polishchuk RS, Polishchuk EV, Marra P, et al. Correlative light-electron microscopy reveals the tubular-saccular ultrastructure of carriers operating between Golgi apparatus and plasma membrane. *J Cell Biol.* 2000;148(1):45-58.
5. Jun S, Ke D, Debiec K, et al. Direct visualization of HIV-1 with correlative live-cell microscopy and cryo-electron tomography. *Structure.* 2011;19(11):1573-1581.
6. Verkade P. Moving EM: the rapid transfer system as a new tool for correlative light and electron microscopy and high throughput for high-pressure freezing. *J Microsc.* 2008;230(2):317-328.
7. Olmos Y, Hodgson L, Mantell J, Verkade P, Carlton JG. ESCRT-III controls nuclear envelope reformation. *Nature.* 2015;522(7555):236-239.
8. Heiligenstein X, Heiligenstein J, Delevoye C, et al. The CryoCapsule: simplifying correlative light to electron microscopy. *Traffic.* 2014;15:700-716.
9. Spiegelhalter C, Tosch V, Hentsch D, et al. From dynamic live cell imaging to 3D ultrastructure: novel integrated methods for high pressure freezing and correlative light-electron microscopy. *PLoS One.* 2010;5(2):e9014.
10. Gaudin R, Berre S, Cunha de Alencar B, et al. Dynamics of HIV-containing compartments in macrophages reveal sequestration of virions and transient surface connections. *PLoS One.* 2013;8(7):e69450.
11. Polishchuk RS, San Pietro E, Di Pentima A, Teté S, Bonifacino JS. Ultrastructure of long-range transport carriers moving from the trans-Golgi network to peripheral endosomes. *Traffic.* 2006;7(8):1092-1103.
12. Titz B, Genoud C. Volume scanning electron microscopy for imaging biological ultrastructure. *Biol Cell.* 2016;108(11):307-323.
13. Horstmann H, Körber C, Sätzler K, Aydin D, Kuner T. Serial section scanning electron microscopy (S 3EM) on silicon wafers for ultra-structural volume imaging of cells and tissues. *PLoS One.* 2012;7(4):1-8.
14. Denk W, Horstmann H. Serial block-face scanning electron microscopy to reconstruct three-dimensional tissue nanostructure. *PLoS Biol.* 2004;2(11):e329.
15. Heymann JAW, Hayles M, Gestmann I, Giannuzzi LA, Lich B, Subramaniam S. Site-specific 3D imaging of cells and tissues with a dual beam microscope. *J Struct Biol.* 2006;155(1):63-73.
16. Kizilyaprak C, Bittermann AG, Daraspe J, Humbel BM. FIB-SEM tomography in biology. *Methods Mol Biol.* 2014;1117:541-558.
17. Peddie CJ, Collinson LM. Exploring the third dimension: volume electron microscopy comes of age. *Micron.* 2014;61:9-19.
18. Xu CS, Hayworth KJ, Lu Z, et al. Enhanced FIB-SEM systems for large-volume 3D imaging. *Elife.* 2017;6:1-36.
19. Narayan K, Danielson CM, Lagarec K, et al. Multi-resolution correlative focused ion beam scanning electron microscopy: applications to cell biology. *J Struct Biol.* 2014;185(3):278-284.
20. Murphy GE, Narayan K, Lowekamp BC, et al. Correlative 3D imaging of whole mammalian cells with light and electron microscopy. *J Struct Biol.* 2011;176(3):268-278.
21. Russell MRG, Lerner TR, Burden JJ, et al. 3D correlative light and electron microscopy of cultured cells using serial blockface scanning electron microscopy. *J Cell Sci.* 2017;130:278-291.
22. Settembre C, Fraldi A, Medina DL, Ballabio A. Signals from the lysosome: a control centre for cellular clearance and energy metabolism. *Nat Rev Mol Cell Biol.* 2013;14(5):283-296.
23. Huotari J, Helenius A. Endosome maturation. *EMBO J.* 2011;30(17):3481-3500.
24. Saftig P, Klumperman J. Lysosome biogenesis and lysosomal membrane proteins: trafficking meets function. *Nat Rev Mol Cell Biol.* 2009;10(9):623-635.
25. Klumperman J, Raposo G. The complex ultrastructure of the endolysosomal system. *Cold Spring Harb Perspect Biol.* 2014;6(10):1-22.
26. Reggiori F, Klumperman J. Lysosome Biogenesis and Autophagy. In: Maxfield FR, Willard JM, Lu S, eds. *Lysosomes: Biology, Diseases, and Therapeutics.* USA: John Wiley & Sons, Inc; 2016:7-31.
27. Mari M, Bujny MV, Zeuschner D, et al. SNX1 defines an early endosomal recycling exit for sortilin and mannose 6-phosphate receptors. *Traffic.* 2008;9(3):380-393.
28. Pols MS, Ten Brink C, Gosavi P, Oorschot V, Klumperman J. The HOPS proteins hVps41 and hVps39 are required for homotypic and heterotypic late endosome fusion. *Traffic.* 2013;14(2):219-232.
29. Murk JLAN, Humbel BM, Ziese U, et al. Endosomal compartmentalization in three dimensions: implications for membrane fusion. *Proc Natl Acad Sci U S A.* 2003;100(23):13332-13337.
30. Van Meel E, Klumperman J. Imaging and imagination: understanding the endo-lysosomal system. *Histochem Cell Biol.* 2008;129(3):253-266.
31. Bright NA, Davis LJ, Luzio JP. Endolysosomes are the principal intracellular sites of acid hydrolase activity. *Curr Biol.* 2016;26(17):2233-2245.
32. Pu J, Guardia CM, Keren-Kaplan T, Bonifacino JS. Mechanisms and functions of lysosome positioning. *J Cell Sci.* 2016;129(23):4329-4339.
33. Falcón-Pérez JM, Nazarian R, Sabatti C, Dell'Angelica EC. Distribution and dynamics of Lamp1-containing endocytic organelles in fibroblasts deficient in BLOC-3. *J Cell Sci.* 2005;118(Pt 22):5243-5255.
34. Peden AA, Oorschot V, Hesser BA, Austin CD, Scheller RH, Klumperman J. Localization of the AP-3 adaptor complex defines a novel endosomal exit site for lysosomal membrane proteins. *J Cell Biol.* 2004;164(7):1065-1076.
35. Pols MS, van Meel E, Oorschot V, et al. hVps41 and VAMP7 function in direct TGN to late endosome transport of lysosomal membrane proteins. *Nat Commun.* 2013;4(May 2012):1361.
36. Makarow M. Endocytosis in *Saccharomyces cerevisiae*: internalization of alpha-amylase and fluorescent dextran into cells. *EMBO J.* 1985;4(7):1861-1866.
37. Sachse M, Urbé S, Oorschot V, Strous GJ, Klumperman J. Bilayered clathrin coats on endosomal vacuoles are involved in protein sorting toward lysosomes. *Mol Biol Cell.* 2002;13(4):1313-1328.
38. Futter CE, Gibson A, Allchin EH, et al. In polarized MDCK cells basolateral vesicles arise from clathrin- γ - adaptin-coated domains on endosomal tubules. *J Cell Biol.* 1998;141(3):611-623.
39. Stoorvogel W, Oorschot V, Geuze HJ. A novel class of clathrin-coated vesicles budding from endosomes. *J Cell Biol.* 1996;132(1-2):21-33.
40. Raiborg C, Grønvold Bache K, Mehlum A, Stang E, Stenmark H. Hrs recruits clathrin to early endosomes. *EMBO J.* 2001;20(17):5008-5021.
41. Klumperman J, Hille A, Veenendaal T, et al. Differences in the endosomal distributions of the two mannose 6-phosphate receptors. *J Cell Biol.* 1993;121(5):997-1010.
42. Yamashiro DJ, Tycko B, Fluss SR, Maxfield FR. Segregation of transferrin to a mildly acidic (pH 6.5) para-golgi compartment in the recycling pathway. *Cell.* 1984;37(July):789-800.
43. Hopkins CR, Trowbridge IS. Internalization and processing of transferrin and the transferrin receptor in human carcinoma A431 cells. *J Cell Biol.* 1983;97(2):508-521.
44. Willingham MC, Hanover JA, Dickson RB, Pastan I. Morphologic characterization of the pathway of transferrin endocytosis and recycling in human KB cells. *Proc Natl Acad Sci U S A.* 1984;81(1):175-179.
45. Sachse M, Ramm G, Strous G, Klumperman J. Endosomes: multipurpose designs for integrating housekeeping and specialized tasks. *Histochem Cell Biol.* 2002;117(2):91-104.
46. Futter CE, Pearse A, Hewlett LJ, Hopkins CR. Multivesicular endosomes containing internalized EGF-EGF receptor complexes mature and then fuse directly with lysosomes. *J Cell Biol.* 1996;132(6):1011-1023.
47. van Deurs B, Holm PK, Kayser L, Sandvig K, Hansen SH. Multivesicular bodies in HEp-2 cells are maturing endosomes. *Eur J Cell Biol.* 1993;61(2):208-224.
48. de Wit H, Lichtenstein Y, Geuze HJ, Kelly RB, van der Sluijs P, Klumperman J. Synaptic vesicles form by budding from tubular extensions of sorting endosomes in PC12 cells. *Mol Biol Cell.* 1999;10(12):4163-4176.
49. Murk JLAN, Posthuma G, Koster AJ, et al. Influence of aldehyde fixation on the morphology of endosomes and lysosomes: quantitative analysis and electron tomography. *J Microsc.* 2003;212(1):81-90.
50. Griffiths G, Hoflack B, Simons K, Mellman I, Kornfeld S. The mannose 6-phosphate receptor and the biogenesis of lysosomes. *Cell.* 1988;52(3):329-341.
51. Murk J-LAN, Lebbink MN, Humbel BM, et al. 3-D structure of multi-laminar lysosomes in antigen presenting cells reveals trapping of MHC II on the internal membranes. *Traffic.* 2004;5(12):936-945.

52. Eskelinen E-L. Fine structure of the autophagosome. *Methods Mol Biol.* 2008;445:11-28.
53. Eskelinen E-L. Maturation of Autophagic vacuoles in mammalian cells. *Autophagy.* 2005;1(1):1-10.
54. Dunn WA. Studies on the mechanisms of autophagy: formation of the vacuole. *J Cell Biol.* 1990;110(June):1923-1933.
55. Liou W, Geuze HJ, Slot JW. Improving structural integrity of cryosections for immunogold labeling. *Histochem Cell Biol.* 1996;106(1):41-58.
56. Griffiths G, Pfeiffer S, Simons K, Matlin K. Exit of newly synthesized membrane proteins from the trans cisterna of the Golgi complex to the plasma membrane. *J Cell Biol.* 1985;101(3):949-964.
57. Friedman PL, Ellisman MH. Enhanced visualization of peripheral nerve and sensory receptors in the scanning electron microscope using cryofracture and osmium-thiocarbohydrazide-osmium impregnation. *J Neurocytol.* 1981;10(1):111-131.
58. Willingham C, Rutherford A. Use of osmium-thiocarbohydrazide-osmium and ferrocyanide-reduced methods contrast and preservation in to. *J Histochem Cytochem.* 1984;32(4):455-460.
59. Raiborg C, Malerød L, Pedersen NM, Stenmark H. Differential functions of Hrs and ESCRT proteins in endocytic membrane trafficking. *Exp Cell Res.* 2008;314(4):801-813.
60. Piper RC, Katzmann DJ. Biogenesis and function of multivesicular bodies. *Annu Rev Cell Dev Biol.* 2007;23(1):519-547.
61. Janvier K, Bonifacino JS. Role of the endocytic machinery in the sorting of lysosome-associated membrane proteins. *Mol Biol Cell.* 2005;16(9):4231-4242.
62. Jordens I, Fernandez-Borja M, Marsman M, et al. The Rab7 effector protein RILP controls lysosomal transport by inducing the recruitment of dynein-dynactin motors. *Curr Biol.* 2001;11(21):1680-1685.
63. Flores-Rodriguez N, Rogers SS, Kenwright DA, Waigh TA, Woodman PG, Allan VJ. Roles of dynein and dynactin in early endosome dynamics revealed using automated tracking and global analysis. *PLoS One.* 2011;6(9):e24479.
64. Wijdeven RH, Janssen H, Nahidiazar L, et al. Cholesterol and ORP1L-mediated ER contact sites control autophagosome transport and fusion with the endocytic pathway. *Nat Commun.* 2016;7(May):11808.
65. Raiborg C, Wenzel EM, Stenmark H. ER-endosome contact sites: molecular compositions and functions. *EMBO J.* 2015;34(1848):1848-1858.
66. Friedman JR, Dibenedetto JR, West M, Rowland AA, Voeltz GK. Endoplasmic reticulum-endosome contact increases as endosomes traffic and mature. *Mol Biol Cell.* 2013;24(7):1030-1040.
67. Alpy F, Rousseau A, Schwab Y, et al. STARD3 or STARD3NL and VAP form a novel molecular tether between late endosomes and the ER. *J Cell Sci.* 2013;126(23):5500-5512.
68. Gatta AT, Levine TP. Piecing together the patchwork of contact sites. *Trends Cell Biol.* 2016;20(8):359-366.
69. Prinz WA. Bridging the gap: membrane contact sites in signaling, metabolism, and organelle dynamics. *J Cell Biol.* 2014;205(6):759-769.
70. Phillips MJ, Voeltz GK. Structure and function of ER membrane contact sites with other organelles. *Nat Rev Mol Cell Biol.* 2015;17(2):69-82.
71. Wu Y, Whiteus C, Xu CS, et al. Contacts between the endoplasmic reticulum and other membranes in neurons. *Proc Natl Acad Sci.* 2017;114(24):E4859-E4867.
72. Gowrishankar S, Yuan P, Wu Y, et al. Massive accumulation of luminal protease-deficient axonal lysosomes at Alzheimer's disease amyloid plaques. *Proc Natl Acad Sci.* 2015;112(28):E3699-E3708.
73. Sardiello M, Palmieri M, di Ronza A, et al. A gene network regulating lysosomal biogenesis and function. *Science.* 2009;325(5939):473-477.
74. Kimura S, Noda T, Yoshimori T. Dissection of the autophagosome maturation process by a novel reporter protein, tandem fluorescent-tagged LC3. *Autophagy.* 2007;3(5):452-460.
75. Bright NA, Gratian MJ, Luzio JP. Endocytic delivery to lysosomes mediated by concurrent fusion and kissing events in living cells. *Curr Biol.* 2005;15(4):360-365.
76. Jongsma MLM, Berlin I, Wijdeven RHM, et al. An ER-associated pathway defines endosomal architecture for controlled cargo transport. *Cell.* 2016;166(1):152-166.
77. Rowland AA, Chitwood PJ, Phillips MJ, Voeltz GK. ER contact sites define the position and timing of endosome fission. *Cell.* 2014;159(5):1027-1041.
78. Eden ER, White IJ, Tsapara A, Futter CE. Membrane contacts between endosomes and ER provide sites for PTP1B-epidermal growth factor receptor interaction. *Nat Cell Biol.* 2010;12(3):267-272.
79. Hiroshi KA. Study of cellular swelling and shrinkage during fixation, dehydration and embedding in various standard media. *J Electron Microscop.* 1962;11(3):135-138.
80. Jensen C, Bajer A. Effects of dehydration on the microtubules of the mitotic spindle. Studies in vitro and with the electron microscope. *J Ultrastruct Res.* 1969;26(5):367-386.
81. Weibel ER, Knight BW. A morphometric study on the thickness of the pulmonary air-blood barrier. *J Cell Biol.* 1964;21(3):367-396.
82. Penttilä A, Kalimo H, Trump BF. Influence of glutaraldehyde and/or osmium tetroxide on cell volume, ion content, mechanical stability, and membrane permeability of Erlich ascites tumor cells. *J Cell Biol.* 1974;63(1):197-214.
83. Nixon-Abell J, Obara CJ, Weigel AV, et al. Increased spatiotemporal resolution reveals highly dynamic dense tubular matrices in the peripheral ER. *Science.* 2016;354(6311):aaf3928.
84. van Bergeijk P, Hoogenraad CC, Kapitein LC. Right time, right place: probing the functions of organelle positioning. *Trends Cell Biol.* 2016;26(2):121-134.
85. Korolchuk VI, Saiki S, Lichtenberg M, et al. Lysosomal positioning coordinates cellular nutrient responses. *Nat Cell Biol.* 2011;13(4):453-460.
86. Pal A, Severin F, Hoepfner S, Zerial M. Regulation of endosome dynamics by Rab5 and huntingtin-HAP40 effector complex in physiological versus pathological conditions. *Methods Enzymol.* 2008;438(7):239-257.
87. Verhoeven K, De Jonghe P, Coen K, et al. Mutations in the small GTP-ase late endosomal protein RAB7 cause Charcot-Marie-Tooth type 2B neuropathy. *Am J Hum Genet.* 2003;72(3):722-727.
88. Hämälistö S, Jäättelä M. Lysosomes in cancer - living on the edge (of the cell). *Curr Opin Cell Biol.* 2016;39:69-76.
89. Mohamed MM, Sloane BF. Cysteine cathepsins: multifunctional enzymes in cancer. *Nat Rev Cancer.* 2006;6(10):764-775.
90. Walton J. Lead an en bloc contrast stain particularly ultrastructural enzymology 'useful for ultrastructural enzymology. *J Histochem Cytochem.* 1979;27(10):1337-1342.
91. Meijering E, Dzyubachyk O, Smal I. Methods for cell and particle tracking. *Methods Enzymol.* 2012;504:183-200.
92. Schindelin J, Arganda-Carreras I, Frise E, et al. Fiji: an open-source platform for biological-image analysis. *Nat Methods.* 2012;9(7):676-682.
93. Cardona A, Saalfeld S, Schindelin J, et al. TrakEM2 software for neural circuit reconstruction. *PLoS One.* 2012;7(6):e38011.
94. Kremer JR, Mastronarde DN, McIntosh JR. Computer visualization of three-dimensional image data using IMOD. *J Struct Biol.* 1996;116(1):71-76.

SUPPORTING INFORMATION

Additional Supporting Information may be found online in the supporting information tab for this article.

How to cite this article: Fermie J, Liv N, ten Brink C, et al. Single organelle dynamics linked to 3D structure by correlative live-cell imaging and 3D electron microscopy. *Traffic.* 2018;19:354-369. <https://doi.org/10.1111/tra.12557>